BIOPHYSICS

Tissue stiffness mapping by light sheet elastography

Min Zhu[1]†, Kaiwen Zhang[1,2]†, Evan C. Thomas[1], Ran Xu[1,3], Brian Ciruna[1,3], Sevan Hopyan[1,3,4]*, Yu Sun[2,5,6]*

Tissue stiffness plays a crucial role in regulating morphogenesis. The ability to measure and monitor the dynamic progression of tissue stiffness is important for generating and testing mechanistic hypotheses. Methods to measure tissue properties in vivo have been emerging but present challenges with spatial and temporal resolution especially in 3D, by their reliance on highly specialized equipment, and/or due to their invasive nature. Here, we introduce light sheet elastography, a noninvasive method that couples low-frequency shear waves with light sheet fluorescence microscopy by adapting commercially available instruments. With this method, we achieved in toto stiffness mapping of organ-stage mouse and zebrafish embryos at cellular resolution. Versatility of the method enabled time-lapse stiffness mapping during tissue remodeling and of the beating embryonic heart. This method expands the spectrum of tools available to biologists and presents opportunities for uncovering the mechanical basis of morphogenesis.

INTRODUCTION

Morphogenesis involves complex coordination of biochemical and biophysical signals. Stiffness, a key mechanical property of tissue, plays a multifaceted role by modulating cell behaviors (*1*–*3*) and interacting with biochemical mediators (*4*–*6*). A holistic understanding of how the distributions and dynamic changes in tissue stiffness contribute to development requires new measurement tools.

Atomic force microscopy (AFM) indentation is a widely used method for measuring two-dimensional (2D) stiffness at the tissue surface (*7*). To measure the stiffness of deeper tissue layers, surgical removal of the surface layer is required (*2*). The few state-of-the-art untethered methods permitting in vivo measurement of 3D tissue stiffness require the injection of magnetic beads or droplets (magnetic tweezers) (*3*, *8*–*10*) or silica beads (optical tweezers) (*11*). These methods are cumbersome, cause potential damage especially to sensitive tissues such as the developing brain and heart, and are limited in spatial resolution that relies on the positions of the deposited beads. Morphogenesis unfolds over time, and invasive techniques fail to capture the temporal dynamics of stiffness, thereby limiting current studies to endpoint analyses. An ideal method would be noninvasive, permit high spatial and temporal resolution, and be sufficiently versatile for a substantial proportion of biologists using commercially available equipment.

Elastography is a noninvasive approach that consists of an actuation component to introduce local tissue deformation and an imaging tool to record the response of the tissue to quantify stiffness (*12*). In terms of actuation principles, current elastography techniques can be categorized into optical and mechanical modes. In Brillouin microscopy (*13*, *14*), the frequency shift of incident laser Brillouin scattering (i.e., Brillouin frequency shift in gigahertz) is used as a proxy for tissue stiffness (i.e., longitudinal modulus) assuming known refractive indices. The relationship between Brillouin microscopy measured longitudinal modulus and elastic modulus (a common metric of tissue stiffness), however, remains unclear. A phenomenological positive correlation between the two quantities (*15*–*17*) and no correlation (*18*) were both reported when benchmarked against AFM indentation. This is potentially due to the fact that Brillouin microscopy naturally couples mechanical and optical properties of each location in a tissue (*13*, *18*). In terms of measurement speed, the acquisition speed of Brillouin microscopy is typically 20 to 500 ms per pixel (i.e., 20 to 500 s for capturing a 1000 by 1000 image) (*14*). To solve the reliance on known refractive indices of different locations in a tissue, Brillouin microscopy has been used together with optical diffraction tomography (*19*), which further lengthens its acquisition time. Moreover, Brillouin frequency shift has been reported to be 10-fold more sensitive to water content than to stiffness (*20*, *21*). Interpreting Brillouin microscopy results in tissues with varying hydration levels requires caution (*13*). Therefore, despite its capability of offering subcellular resolution, Brillouin microscopy is suboptimal for stiffness mapping of 3D tissue comprising multiple slices.

For mechanically actuated elastography, compression optical coherence elastography (C-OCE) and wave-based elastography have been developed (*22*). C-OCE, which is based on local strain imaging under axial (depth) compression (*23*–*25*), relies on known refractive indices and has reduced accuracy and sensitivity when measuring tissues lacking mechanical stiffness contrast (*22*, *26*). For quantitative stiffness measurement, uniform stress is assumed, which introduces errors in mapping geometrically complex tissues with variable stress (*22*, *25*). C-OCE also has limited axial resolution for strain measurement (~300 μm) in tissues (*25*). In wave-based elastography, the propagation speed of a shear wave is proportional to tissue stiffness (*27*). This approach has been applied clinically using ultrasound elastography and 2D/3D magnetic resonance elastography for diagnosing stiffness-related diseases such as liver fibrosis (*28*, *29*). Switching the imaging modality to optical microscopy has improved spatial resolution. However, a high actuation frequency in the kilohertz range has been required to enhance local phase contrast for generating an observable phase shift to calculate shear wave propagation speed. This requirement arises from limited displacement tracking

[1]Program in Developmental and Stem Cell Biology, Research Institute, The Hospital for Sick Children, Toronto, ON, M5G 0A4, Canada. [2]Department of Mechanical and Industrial Engineering, University of Toronto, Toronto, ON, M5S 3G8, Canada. [3]Department of Molecular Genetics, University of Toronto, Toronto, ON, M5S 1A8, Canada. [4]Division of Orthopaedic Surgery, The Hospital for Sick Children and University of Toronto, Toronto, ON, M5G 1X8, Canada. [5]Institute of Biomedical Engineering, University of Toronto, Toronto, ON, M5S 3G9, Canada. [6]Department of Electrical and Computer Engineering, University of Toronto, Toronto, ON, M5S 3G4, Canada.
*Corresponding author. Email: sevan.hopyan@sickkids.ca (S.H.); yu.sun@utoronto.ca (Y.S.)
†These authors contributed equally to this work.

under bright-field imaging with particle imaging velocimetry (*30*). Capturing sample response to such high-frequency actuation makes it incompatible with confocal or light sheet imaging and obviates 3D stiffness mapping. The high frequency actuation also leads to rapid amplitude attenuation, impeding whole embryo penetration.

To tackle these limitations, we developed a method for mapping stiffness by coupling mechanical actuation with light sheet fluorescence microscopy (table S1). A standard piezoelectric device was used to propagate shear waves through organ-stage mouse embryos (~3 mm). The shear wave displaced cells that were individually visualized by a transgenic far-red nuclear reporter H2B-miRFP703 (*31*) that offered high-contrast and deep tissue imaging. Application of a customized pattern-guided cell motion tracking program enabled accurate reconstruction of local displacement patterns and distinguished phase shifts as low as 0.0023 rad at a low actuation frequency (≤10 Hz). We achieved whole embryo shear wave penetration and in toto tissue stiffness mapping at cellular (15 μm) resolution with time-lapse capability. Stiffness of the beating embryonic heart during ventricular contraction and relaxation was also mapped for the first time.

RESULTS

Light sheet elastography device

To optimize live imaging for mouse embryos, our device was built on a standard light sheet fluorescence microscope that provides high spatiotemporal resolution and minimizes photobleaching. Simultaneous planar laser excitation and acquisition enabled by light sheet microscopy mitigated the confounding delay for specimen scanning (illuminating) by confocal microscopes. The light sheet elastography (LSE) device consisted of a standard piezoelectric actuator (P-840.20, Physik Instrumente) that vibrated with displacement of up to ~30 μm perpendicular to a capillary tube housing an agarose plug. Piezoelectric actuation by a sinusoidal signal generated a shear wave through the agarose plug and the embryo embedded within it (Materials and Methods). A mounting stage was secured to the microscope sample stage by permanent magnets (Fig. 1, A and B).

Dynamic phase analysis

Under ideal pure shear actuation as illustrated in Fig. 1C and movie S1, the local shear modulus G relates to local phase difference by (*27*)

$$G = \rho {c_s}^2 = \rho \left(\frac{2\pi f}{\Delta\varphi/\Delta y} \right)^2 \quad (1)$$

where ρ is the density, c_s is the shear wave propagation speed, f is the actuation frequency, and $\Delta\varphi / \Delta y$ is the Y phase gradient. The relationship was based on the principle that a forward-propagating wave passes specified point locations with a phase delay. For two points along the path of a shear wave that are in close proximity such that the material in between them can be considered homogeneous, the difference in the local phases at the two points was used to calculate the stiffness of the material between the two points. The local shear modulus G is related to elastic modulus E (a common metric for describing tissue stiffness) by

$$E = 2(1+\upsilon)G \quad (2)$$

where υ is the Poisson's ratio which is typically 0.5 for soft tissue (*9*, *32*).

In addition to the phase arising from pure shear wave propagation, other potential contributors to the phase of the extruded agarose gel are the phase inherited from the glass capillary above the gel, the damping effect of the culture medium, and the geometry (i.e., diameter and extrusion length) of the gel (Fig. 1D and Supplementary Note).

To validate the phase-stiffness equation and evaluate the effect of potential contributing factors, we conducted shear wave actuation on 1% agarose gel that contained fluorescent beads. By tracking the displacement of the beads and fitting with the sinusoidal equation to decouple phase values (Materials and Methods), we obtained a local phase map of 1% agarose gel (Fig. 1E). The phase map decays linearly along Y due to shear wave propagation with an average Y phase gradient of 51.8 rad/m (Fig. 1F). In addition to the Y phase, the phase also shows a linear symmetric decay along X with a ruffle fold that is inherited from the agarose gel inside the glass capillary (Fig. 1G). The decay and ruffle fold resulted from wave propagation in the poroelastic material arising from the glass-gel boundary and wave interference, respectively (fig. S1A and Supplementary Note) (*33*). Inside the glass capillary, the agarose gel phase map exhibited the same X phase pattern as the extruded part without Y phase decay (fig. S1, B to D). This X phase pattern was experimentally determined to be independent of Z location, glass capillary diameter, and agarose gel concentration (fig. S1, E to G). The X phase speed (i.e., wave propagation speed) remained constant across different actuation frequencies, suggesting that the wave was nondispersive (fig. S1H).

The extruded gel was found to be critically damped (i.e., damping ratio close to 1) by Dulbecco's modified Eagle's medium (DMEM; fig. S2A and Supplementary Note). The critical damping effect filters out undesired wave reflection and mitigates its contribution to the local phase under forced oscillation (*27*). DMEM damping arose from the added mass of the fluid that was displaced by the agarose gel and viscous fluid shear. From experimental and numerical simulation results, DMEM damping was dominated by mass damping (fig. S2, B to F). Replacing the culture medium with fluids of different viscosities did not affect the phase result, as they all had a similar density to water. The critical damping effect extended to agarose gels of different elastic moduli and diameters (fig. S2, G and H). We further verified that the rotational bending and deflection induced by the agarose gel's geometry were minimal and can be disregarded for phase analysis (fig. S2, I to L, and Supplementary Note). By performing actuation at different frequencies, Y phase speed was found to be constant (i.e., nondispersive) as depicted in fig. S2M, indicating the predominantly elastic behavior of the agarose gel. The elastic behavior of agarose gel was recapitulated by AFM indentation (fig. S3A and Materials and Methods).

Hence, the phase in the extruded agarose gel was solved according to

$$\varphi = \varphi_x + \varphi_y = k_x \cdot |x| + k_s y = -2.25 f |x| + \frac{\partial \varphi}{\partial y} y \quad (3)$$

where k_x and k_s are the X and Y wave numbers, respectively (Supplementary Note). Using our customized dynamic phase program (code link in Materials and Methods), the partial derivative of phase with respect to Y was computed, and the stiffness of 1% agarose gel was decoupled (Fig. 1H) and determined to be 4.1 kPa on average for this gel sample. To validate LSE-measured stiffness, we compared the stiffness of 0.75 to 3% agarose gels quantified by LSE and by AFM indentation (fig. S3, B and C). LSE-measured

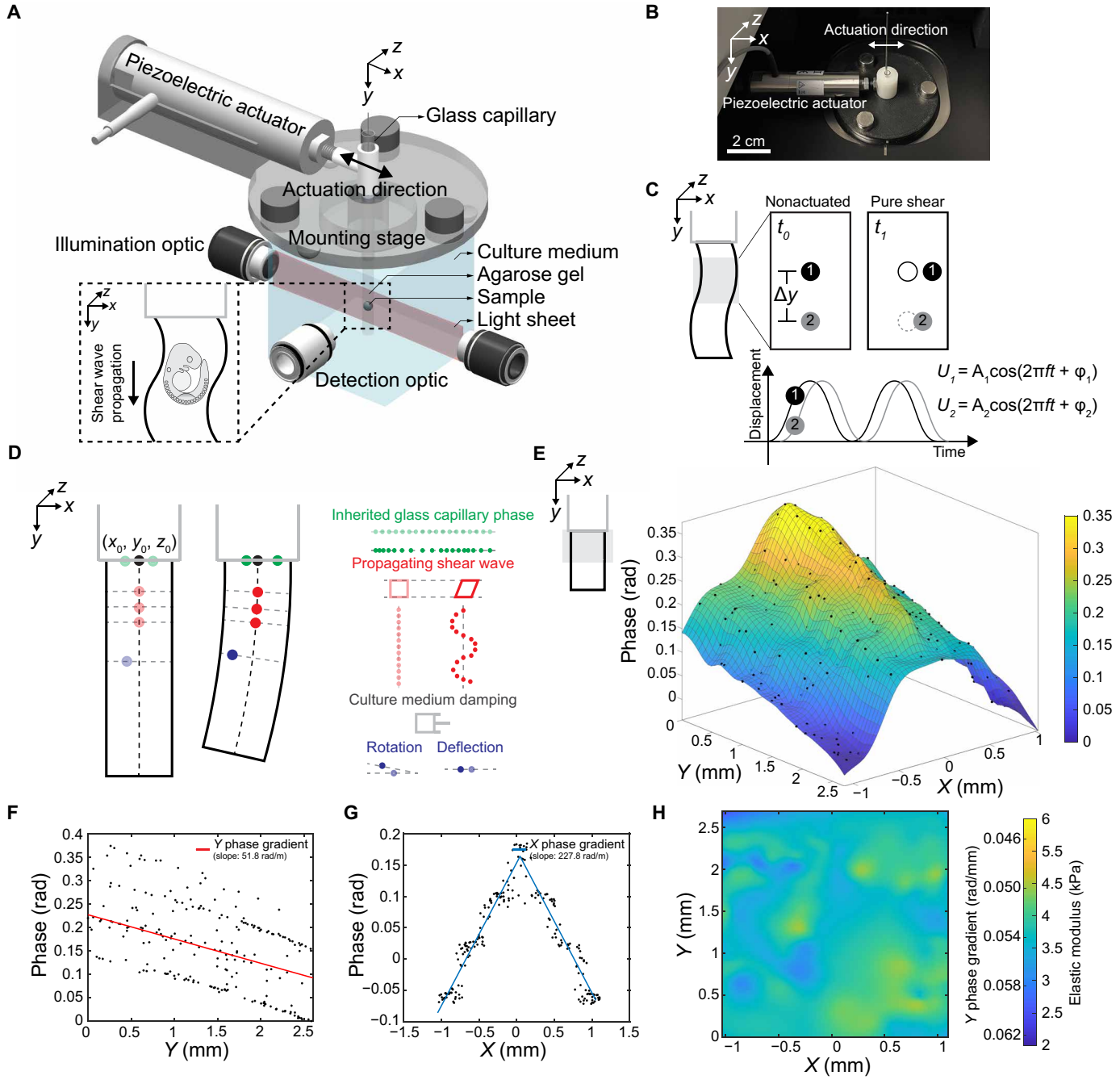

Fig. 1. Light sheet elastography. (**A**) 3D structure of the LSE device. (**B**) Experimental setup of LSE. (**C**) Schematic illustrating ideal pure shear wave propagation causing a phase delay along the *Y* axis. (**D**) Schematic describing potential contributors to the local phase. (**E**) 3D rendered phase map of 1% agarose gel under 10-Hz actuation. (**F**) *YZ* projection of the phase map shown in (E) showing linear phase decay induced by shear wave propagation along the *Y* axis. (**G**) Inherited glass capillary phase along the *X* axis. (**H**) Stiffness map of 1% agarose gel. The spatial variation reflects the heterogeneous distribution of agarose fibers during sample preparation (Materials and Methods). Color-coded scale showing elastic modulus and its corresponding *Y* phase gradient under 10-Hz actuation.

stiffness values of agarose gel agreed well with AFM indentation results for gel concentrations ranging from 0.75 to 2% (i.e., <~10 kPa) with differences less than 7.4%. For 3% agarose gel, LSE-measured values deviated from AFM indentation results by 20.9%. This discrepancy occurred because the frame rate of the Zeiss Z.1 light sheet microscope at 1000 × 1000 pixels was unable to capture the rapid propagation of shear waves to decouple the *Y* phase gradient in the stiff gel. For measuring stiff samples, the LSE pixel setting can be lowered to increase the frame rate. For 3% agarose gel, lowering the pixel setting from 1000 × 1000 to 250 × 250 enabled LSE to reproduce AFM indentation results (within 7.2% difference and reduced variance) at the cost of a smaller field of view.

To simulate a heterogeneous stiffness environment, we also conducted validation on gradient agarose gels with spatially varying stiffness (fig. S3D and Materials and Methods). For 1 to 2% gradient agarose gel, LSE measured continuous points and resolved the stiffness gradient to within 7.7% difference compared to AFM indentation (fig. S3, E and F).

In toto tissue stiffness mapping

To achieve maximum imaging penetration depth, we performed tissue stiffness mapping of an E9.25 (embryonic day 9.25) mouse embryo using a transgenic mouse strain harboring a far-red nuclear reporter H2B-miRFP703 (*31*). This mouse line has been useful in various live imaging studies as it allows clear visualization throughout tissue with minimal phototoxicity (*3*, *6*, *34*). To track the fast moving, densely populated nuclei under shear wave propagation, we developed a motion tracking program using a subpixel image registration algorithm (figs. S4, A to D, and S5A; movie S2; and code link in Materials and Methods) (*35*), capable of resolving a phase shift as small as 0.0023 rad (Materials and Methods). At E9.25, the mouse embryonic heart regularly beats at ~2 Hz (Fig. 2A and movie S3) with an amplitude that extends to ~200 μm away from the heart (fig. S5B). To compensate for the heartbeat, we chose our actuation frequency to be distinct from that of the beating frequency and eliminated the heartbeat signal using bandpass filtering (fig. S5A). The time resolution of LSE (i.e., number of frames required for a stable phase reading) was determined to be 7 frames (0.12 s) (fig. S5C). The spatial resolution was calculated as a function of the time resolution, actuation frequency, and sample stiffness considering a minimum signal-to-noise ratio of 3 (Materials and Methods). Within the stiffness range of most embryonic tissues (a few hundred pascals), neighboring cells' phase difference could be resolved by LSE yielding cellular resolution (<15 μm) for stiffness mapping (fig. S5, D to F, and Supplementary Note). The cellular spatial resolution and subsecond temporal resolution of LSE are comparable to those of existing optical elastography methods (*30*, *36*, *37*) but were achieved at a much lower frame rate (~50 Hz) compared to the multikilohertz frequency of those methods. The spatiotemporal resolution of LSE can be further improved by increasing the imaging frame rate of the light sheet microscope. No notable changes in cell apoptosis were observed after LSE actuation as examined by LysoTracker staining (fig. S5G and Materials and Methods).

The stiffness of E9.25 mouse embryos was mapped by stitching sagittal plane tiles as shown in Fig. 2 (B and C). The void areas in the stiffness map are cavities filled with intraembryonic fluid. Since shear waves do not propagate through fluid (*38*), cavities do not affect stiffness mapping results. The E9.25 embryo exhibited a stiff forebrain, hindbrain, and somites with comparatively soft midbrain and optic vesicle regions. We compared LSE with established in vivo stiffness measurement methods. LSE results agreed well with previously reported values for the E9.25 mandibular arch, mouse forelimb bud, and the tailbud of 16 hours postfertilization (hpf) zebrafish harboring an mScarlet nuclear reporter (*39*) that were measured using AFM indentation (*7*, *40*) and magnetic tweezers (*3*, *8*, *10*) but with greater spatial detail (Fig. 2, D and E, and fig. S5, H and I).

Cell packing density and extracellular matrix (ECM) composition are regarded as two major contributing factors of tissue stiffness (*3*, *6*, *41*). Both parameters vary spatially during development. By crossing the nuclear reporter H2B-miRFP703 strain with our endogenous fibronectin (FN; a major ECM protein) reporter strain (Fn-mScarlet) (*6*), we explored the potential contributions of these two factors to stiffness (Fig. 2F and Materials and Methods). Some regions of high stiffness by LSE such as the hindbrain and somites corresponded spatially to high cell packing density, whereas others in the mandibular arch and forelimb bud matched FN gradients (Fig. 2G). It will be interesting to determine how different determinants of tissue stiffness affect morphogenesis.

Time-lapse tissue stiffness mapping

The noninvasive nature of LSE enabled time-lapse tissue stiffness mapping. We previously discovered an anteriorly biased tissue stiffness gradient in the mouse E9.25 forelimb bud by taking single time point measurements per embryo (*3*). In contrast, LSE enabled time-lapse stiffness mapping over a 3-hour period. During that period, the stiffness gradient evolved such that the anterior bias expanded toward the central region (Fig. 2H). That progression is consistent with an anterior to central transition of the distal peak of the limb bud as it expands between E9.25 and E9.5 (*3*, *6*). The ability to observe live changes in tissue stiffness may be useful for defining the basis of morphogenetic movements.

The noninvasive nature of LSE also allowed for stiffness mapping of mechanosensitive tissues such as the beating embryonic heart that cannot be achieved by existing methods. Experiments confirmed that 10-Hz LSE actuation for 1.7 s (i.e., 100 frames) did not induce any heartbeat frequency change or arrhythmia (Fig. 3A). An important aspect of measuring heart stiffness is that shear wave propagation speed is affected by tissue stress (*42*). To differentiate heart stiffness during ventricular relaxation and contraction, we first measured the time weighted average (>10 heartbeats) of E9.25 heart stiffness as shown in Fig. 3 (B and C). A time resolution of 0.12 s (i.e., 7 frames) allowed us to isolate stiffness during ventricular relaxation as shown in Fig. 3D. Heart stiffness during ventricular contraction was decoupled according to

$$E_{\text{heart}} = \frac{E_{\text{relax}} \cdot t_{\text{relax}} + E_{\text{contract}} \cdot t_{\text{contract}}}{t_{\text{relax}} + t_{\text{contract}}} \tag{4}$$

and was 23.2% higher than in the relaxed state (Fig. 3, E and F). Whether the heartbeat increases or decreases, the apparent stiffness depends on tissue stress which is determined by the superposition of contractile stress upon initial stress in the relaxed state. An analogy would be stretching (increase) or releasing (decrease) a prestressed rubber band. Since LSE can distinguish contributions of contractile stress to stiffness throughout the cardiac cycle, the method can potentially identify the precise functional consequences of deleterious mutations.

The formation of trabeculae is a key step in cardiac development, and disorders of that process lead to cardiomyopathy and embryonic lethality (*43*, *44*). According to image-based simulations, trabeculae act like structural supports that enhance cardiac wall deformability, reduce fluid pressure stresses, and homogenize wall stiffness (*45*). Their formation is mechanosensitive, but emerging models of trabeculation that invoke tissue properties have thus far been based largely on inference from imaging and theory (*46*–*49*).

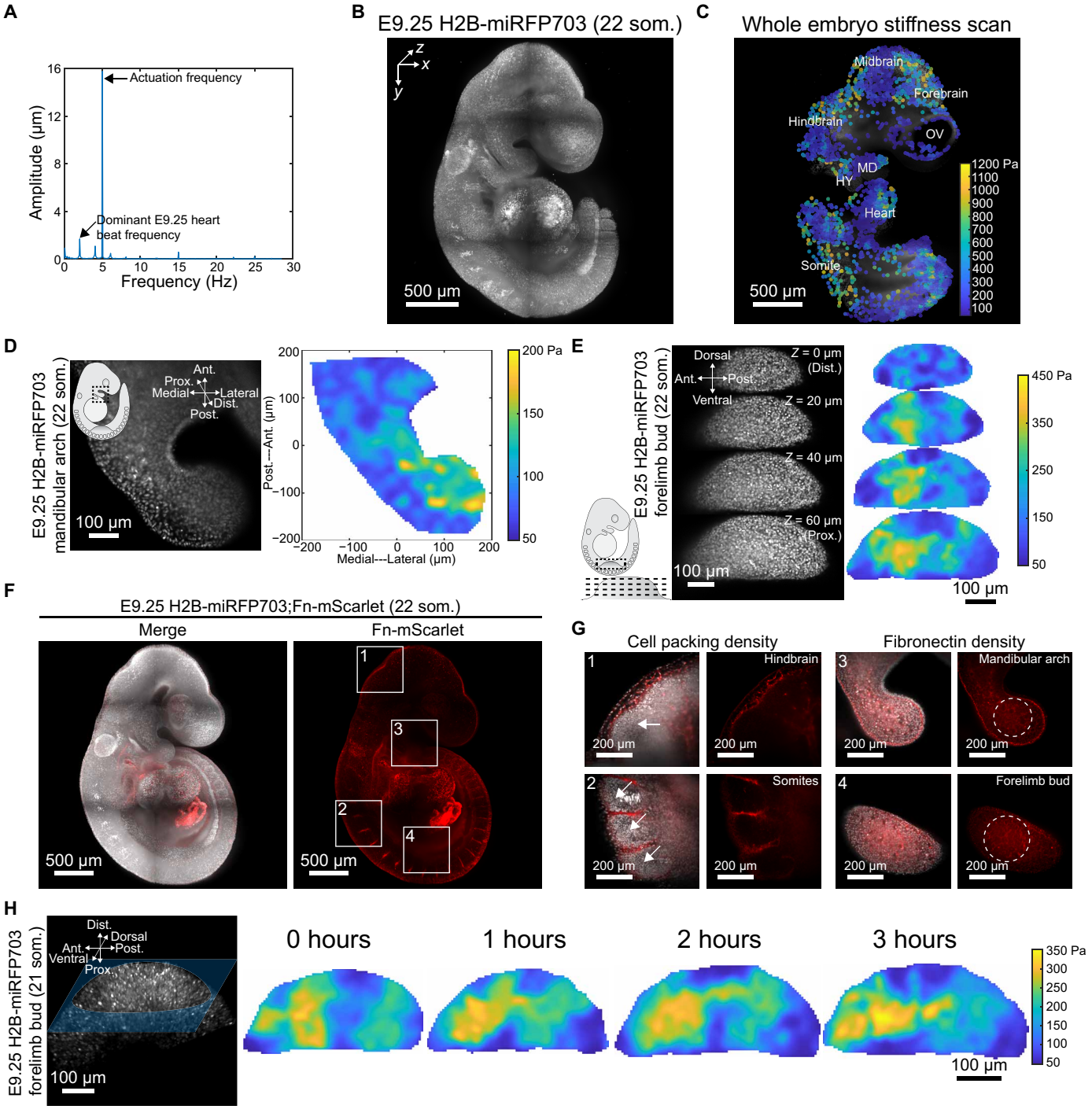

Fig. 2. Noninvasive tissue stiffness mapping. (**A**) Fast Fourier transform of a heart cell under 5-Hz actuation. (**B**) 3D rendering of an E9.25 H2B-miRFP703 mouse embryo. (**C**) Slice view of a E9.25 whole embryo stiffness map. In this wide-field depiction of six stitched tiles of 15-μm resolution stiffness data, a subset of data points is shown as individual dots for easy of visualization. OV, optic vesicle; MD, mandibular arch; HY, hyoid arch. (**D**) Slice view of color map rendered E9.25 mandibular arch stiffness. (**E**) Slices at different depths of E9.25 limb bud 3D stiffness map. (**F**) 3D rendering of an E9.25 H2B-miRFP703;Fn-mScarlet mouse embryo. (**G**) Contributing factors of tissue stiffness in different regions [solid squares in (F)]. Left illustrating high cell packing density (arrows) leads to the stiff hindbrain and somites (som.) as shown in (C). Right illustrating FN density (dashed circles) modulates stiffness gradient observed in mandibular arch (D) and forelimb bud (E). (**H**) Time-lapse stiffness map of an E9.25 limb bud.

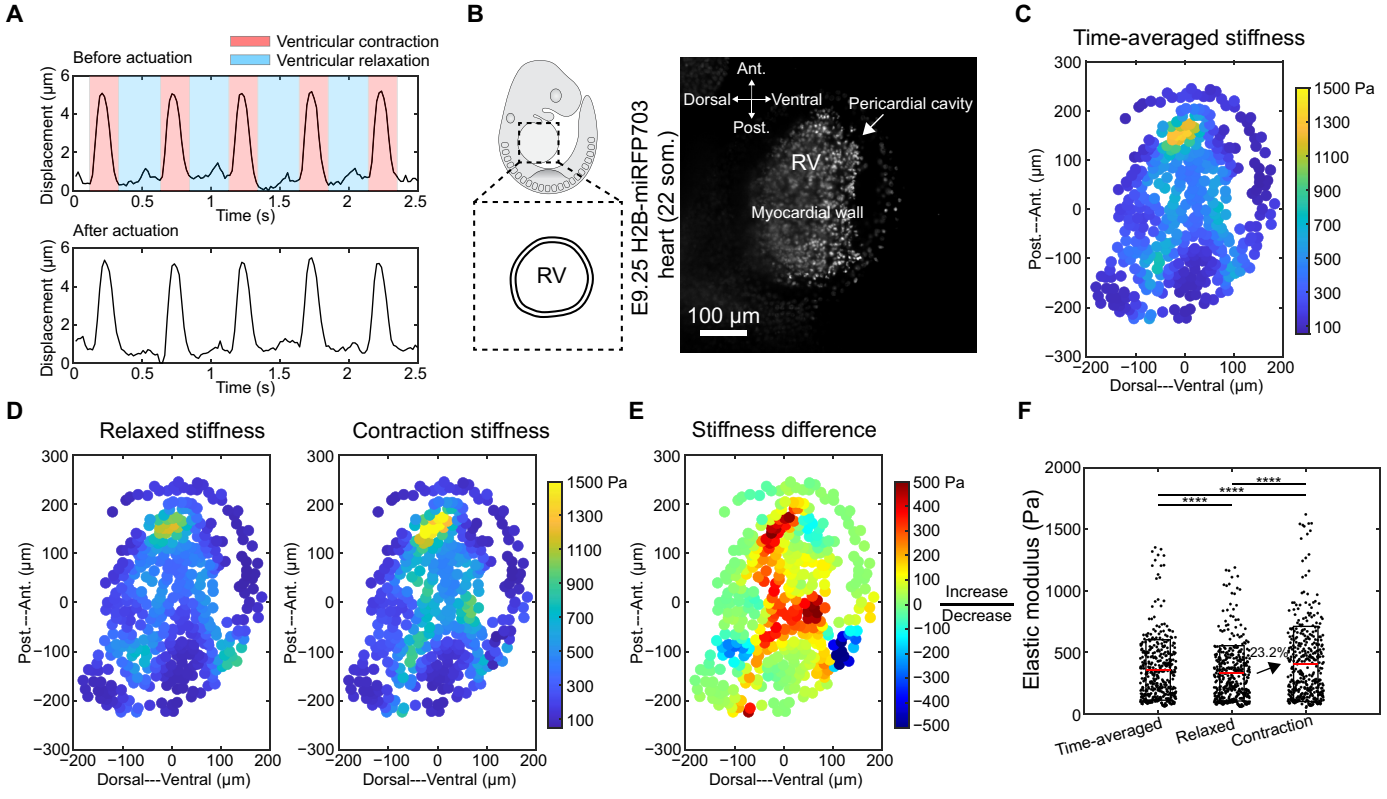

Fig. 3. Heart stiffness mapping. (**A**) Heart nuclear displacements by tracking nuclei before and after actuation showing no changes in beating frequency and rhythm. (**B**) Slice view of an E9.25 H2B-miRFP703 embryonic heart showing the focal plane of stiffness mapping. RV, right ventricle. (**C**) Time-averaged heart stiffness map. (**D**) Heart stiffness mapped during ventricular relaxation and decoupled ventricular contraction stiffness map. (**E**) Heart stiffness difference between ventricular relaxation and contraction. The stiffness pattern in (C) to (E) is likely due to the FN composition near the trabeculae, as shown in the next figure. (**F**) Box plot showing time-averaged, relaxed, and contraction-phase heart stiffness (two-tailed paired Student's *t* test, ****$P < 0.0001$).

As proof of principle of the value of LSE, we mapped trabecular stiffness to generate a morphogenetic hypothesis (Fig. 4, A to C). An apical to basal stiffness gradient was observed within each trabecula of the E9.25 left ventricle. The stiffness gradient was found to correspond to FN density (Fig. 4, D and E), raising the possibility that myocardial cells move up the stiffness gradient, a process akin to durotaxis, to raise the structure from the cardiac wall (Fig. 3F). An increasing number of trabecular cells would increase the production of ECM proteins, potentially feeding back positively upon cell movement into trabeculae until the degree of their stiffness precludes further cell migration similar to what has been observed in limb bud mesoderm (*6*). These and other models can be rigorously tested by combining live imaging and genetic approaches with LSE.

DISCUSSION

Noninvasively mapping 3D tissue stiffness by LSE offers the potential for a panoramic view of tissue stiffness among various embryos at different stages of development at a spatiotemporal resolution of 15 μm and 0.12 s. Higher temporal resolution can be achieved by increasing the image frame rate at the cost of the field of view. Higher spatial resolution can be achieved in soft tissues, by lowering time resolution or increasing actuation frequency, provided the imaging frame rate is sufficient for precise displacement tracking. With a readily replicable setup, LSE is amenable for integration with a standard light sheet microscope or a custom-built affordable light sheet microscope (*50*). The noninvasive nature of this method also enables tissue stiffness mapping over time during development. LSE combined with live imaging of molecular reporters permits simultaneous visualization of biomechanical and biochemical interactions in vivo, offering the potential to resolve "chicken-and-egg" questions in morphogenesis. Temporal progression of tissue stiffness also provides valuable inputs for computational modeling and simulation of morphogenetic events. The limitations of LSE stem from the Zeiss Z.1 microscope specifications. The Zeiss Z.1 can accommodate a sample up to a 1-ml syringe with an inner diameter of 4.76 mm, and its frame rate is limited by a minimum exposure time of 7 ms. While this frame rate is sufficient for mapping embryonic tissue stiffness, a higher frame rate is needed for applications requiring subcellular resolution or imaging of stiff adult tissues which could potentially be achieved by switching to a lattice light sheet microscope or a customized high-speed light sheet microscope, respectively (*51*).

The major limitation of LSE lies in the laser penetration depth of the H2B-miRFP703 reporter, which is ~500 μm (*34*, *52*). Although deeper penetration could be achieved by switching to multiphoton imaging, the imaging speed would be compromised, resulting in a trade-off between penetration depth and spatiotemporal resolution. In our application of LSE, we relied on live fluorescent reporters with high local contrast to achieve precise displacement tracking for phase analysis. For animal models in which transgenic fluorescent

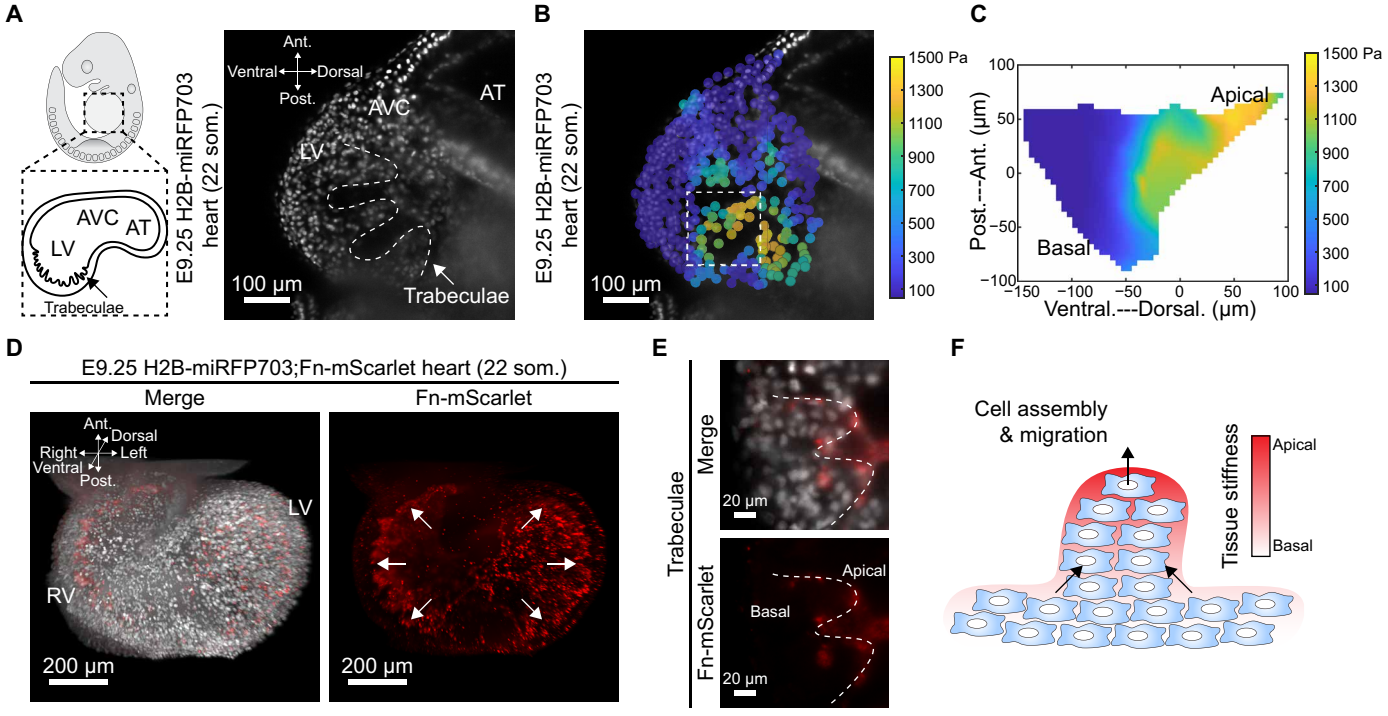

Fig. 4. Ventricular trabeculation. (**A**) Slice view of an E9.25 H2B-miRFP703 embryonic heart illustrating ventricular trabeculation. (**B**) Trabecular myocardium stiffness map at the focal plane shown in (A). (**C**) Rendered zoom-in trabecular myocardium stiffness map [dashed square in (B)]. (**D**) 3D rendering of an E9.25 H2B-miRFP703;Fn-mScarlet embryonic heart. Arrows indicate ventricular trabeculation. (**E**) Zoom-in view of FN expression in trabecular myocardium (dashed line). (**F**) Schematic model representing the potential mechanism that underlies ventricular trabeculation. AT, atria; AVC, atrioventricular canal; LV, left ventricle; RV, right ventricle.

reporters are not available, vital fluorescent dyes, pigment cells that have high local contrast under bright-field imaging, differential interference contrast microscopy, or phase contrast imaging where they are available may be possible alternatives for performing LSE.

In cardiac research, tissue stiffness has been invoked but not measured directly in vivo due to a lack of quantification tools. LSE's ability to map stiffness throughout the cardiac cycle and during the morphogenesis of various organ primordia opens avenues for proposing and testing hypotheses concerning development and congenital disease in vivo or in vitro using organoid models (*53*). LSE is compatible with imaging-based mechanical strain mapping (*7*, *54*). Since the product of stiffness and strain yields stress, cardiac tissue stress can be spatiotemporally monitored by computing the product of the stiffness and strain maps. The fast-imaging speed of light sheet microscopy also permits the capture of cardiac conduction velocity (tens of centimeters per second) (*55*). LSE therefore offers the potential for comprehensive cardiac mechanical assessment by simultaneously quantifying cardiac stiffness, stress, and conduction velocity.

An opportune potential application is that LSE makes it possible to register single-cell transcriptomic and proteomic datasets spatially with physical properties. Another is that, aside from measurements, actuation of LSE with higher energy offers the potential to manipulate shear stress. Since shear stress can activate signaling cascades that affect morphogenesis (*56*, *57*) and disease progression (*58*, *59*), LSE can be actuated to test mechanotransduction hypotheses. Our hope is that LSE will render a subset of mechanobiology experiments technically accessible for standard biology labs at low cost.

MATERIALS AND METHODS

Animal strains

Analysis was performed using the mouse strain R26-CAG-H2B-miRFP703 [The Jackson Laboratory: Gt(ROSA)26Sor$^{em1.1(CAG-RFP*)Jrt}$/J] and Fn-mScarlet (*6*), outbred to CD1. The zebrafish analysis was performed using Tg(ubi:loxp:mScarlet-nls:loxp:QFGal4) (*39*), outbred to Tübingen. All animal experiments were performed in accordance with Canadian Council on Animal Care (CCAC) guidelines, and protocols (1000059338) were approved by the Hospital for Sick Children Research Institute Animal Care Committee.

LSE device

The piezoelectric actuator used in this work is P-840.20 (Physik Instrumente). It was attached to the light sheet microscope (Zeiss Lightsheet Z.1) via a mounting stage that was 3D printed using acrylonitrile butadiene styrene. Three permanent magnets (McMASTER-CARR, lot 5862k178) were used to secure the mounting stage to the Z.1 motorized sample stage. The glass capillary and plunger are standard components for the Z.1. Customized glass capillary holders were 3D printed from resin to connect the glass capillary and actuator. A simple sinusoidal waveform, generated by a function generator (B&K Precision, lot 4053B) and amplified by a custom-made voltage amplifier, was used to drive the piezoelectric actuator. The custom-made voltage amplifier provides a maximum voltage output of 100 V, enabling a travel range of up to 30 μm for the piezoelectric actuator. The design files of the mounting stage, the glass capillary holder, and the voltage amplifier are available for download at https://github.com/MinZhuUOTSickKids/light_sheet_elastography.

Agarose gel validation

To validate LSE, we performed stiffness mapping of 0.75 to 3% low melting point agarose gel (Thermo Fisher Scientific, lot 16520050) in DMEM without phenol red and compared the results to those obtained with AFM indentation. The agarose gel solution contained 5% fluorescent beads of 2 μm in diameter (1:200; Sigma-Aldrich, lot L3030 and L4655). The gradient agarose gel was prepared using a diffusion-based method (*60*) by mixing agarose of two different percentages containing green and red fluorescent beads, respectively. A 2% agarose gel was aspirated into a glass capillary and solidified at room temperature, while a 1% agarose gel solution was kept in a microcentrifuge tube at 95°C. The glass capillary, containing the 2% agarose gel, was submerged 2 mm into the tube for 20 s, followed by aspiration of the 1% agarose gel. The glass capillary was then maintained in a vertical orientation for agarose gel solidification. Once the agarose solidified, the glass capillary was submerged into the imaging chamber containing DMEM without phenol red, and the agarose plug was partially extruded from the glass capillary. The temperature of the imaging chamber was maintained at 37°C with 5% CO_2. Upon actuation, the displacements of the fluorescent beads were tracked using Imaris (Bitplane) and fitted in MATLAB (MathWorks) to obtain the phase map. The stiffness map of the agarose gel was resolved from the phase map by computing the phase decay along *Y* axis.

The stiffness of the same batch agarose gel was also evaluated by AFM (Bruker BioScope Catalyst) mounted on an inverted microscope (Nikon Eclipse-Ti) at 37°C with 5% CO_2. For the average stiffness validation experiment (fig. S3, A to C), the same batch of agarose was poured into a petri dish for AFM indentation. For the gradient gel validation, the gel sample used in LSE was transferred to a petri dish and immobilized by pinning it to the adjacent 4% agarose gel blocks using pulled glass needles, as shown in fig. S3F. A spherical probe tip with a diameter of 32 μm was used for all indentations performed. The spherical tip was made by assembling a borosilicate glass microsphere onto a tipless AFM cantilever using epoxy glue. After assembly, the diameter of the probe tip was measured under a scanning electron microscope (Hitachi 4000). The spring constant of the cantilever was calibrated by measuring the power spectral density of the unloaded cantilever thermal noise fluctuation. For average stiffness validation, AFM indentation was performed at multiple locations spanning the entire surface of the agarose gel. For gradient gel validation, AFM indentation was performed at 200-μm intervals along the gradient direction. The linear regime of the approach curve of each indentation was fitted with the hertz model for a spherical tip to obtain stiffness values (*61*).

Time-lapse tissue stiffness mapping

Dissected embryos were suspended in a solution of DMEM without phenol red containing 12.5% filtered rat serum, 1% low-melt agarose (Thermo Fisher Scientific, lot 16520050), and 1% fluorescent beads (1:500; Sigma-Aldrich, lot L3030) that were used for drift compensation within a glass capillary. The 1% agarose gel was prepared by diluting 4% agarose gel to 1% with DMEM and rat serum to reach the gelling temperature while preserving the stability of the culture medium. Once the agarose solidified, the capillary was submerged into an imaging chamber containing DMEM without phenol red, and the agarose plug was partially extruded from the glass capillary tube until the portion containing the embryo was completely outside of the tube. The temperature of the imaging chamber was maintained at 37°C with 5% CO_2. Images were acquired for 3 to 4 hours at 5-min intervals.

Pattern-guided cell motion tracking program

The tracking function in Imaris (Bitplane) is not applicable to the densely populated and fast-moving cells in the LSE embryo dataset as shown in movie S2. On the basis of Python, we developed a pattern-guided cell motion tracking program for tracking these cells, using a subpixel image registration algorithm (*35*). The algorithm compares two images and computes the pixel translation between them by maximizing intensity correlation with respect to translation in the two directions.

To evaluate the tracking accuracy, randomly distributed 24 Gaussian blobs of one pixel width each were generated and oscillated with an amplitude similar to LSE actuation (i.e., 15 μm) for 128 time points. The synthetic data were imported into our tracking program, and tracking accuracy was quantified by calculating the difference between the real and tracked positions with respect to how far each point moved between each pair of neighboring time points. The tracking accuracy was determined to be 0.35 pixels permitting the detection of phase shifts as small as 0.0023 rad.

With a user interface, our program allows the selection of a working area to track the average motion. It then tracks selected points within the working area by comparing small areas around each point over time. The points themselves and size of the areas around the points to be tracked are user selectable. The output is the positions of the selected points at each time point. The tracking program and synthetic data generator are available for download at https://github.com/MinZhuUOTSickKids/light_sheet_elastography.

Spatiotemporal resolution of LSE

The time resolution was determined by fitting varying numbers of frames to the sinusoidal function $A\cos(\omega t+\varphi)$. We fitted 3 to 100 frames at an interval of 1 frame. The phase reading was found to stabilize after seven frames (fig. S5C). To evaluate the spatial resolution of LSE, we quantified the phase root mean square (RMS) level as a measure of noise, as shown in fig. S5D. The phase RMS is inversely related to time resolution by a power law relation.

Considering a signal-to-noise ratio of 3, the minimum phase shift (0.0023 rad at 100 frames as shown in fig. S5D) that can be differentiated by LSE versus time resolution is

$$\Delta\varphi = 3\varphi_{\mathrm{RMS}} = 0.07425 t_{\mathrm{reso}}{}^{-0.7597} \tag{5}$$

By rewriting the shear modulus-phase shift equation

$$\frac{\Delta\varphi}{\Delta y} = 2\pi f\sqrt{\frac{\rho}{G}} = 2\pi f\sqrt{\frac{2(1+\upsilon)\rho}{E}} \tag{6}$$

and substituting values in the equation, the spatial resolution of LSE (Δy) in microns is

$$s_{\mathrm{reso}} = \Delta y = \frac{215.75\sqrt{E}}{f\cdot t_{\mathrm{reso}}{}^{0.7597}} \tag{7}$$

Thus, the spatial resolution at 10-Hz actuation is shown in fig. S5E.

Apoptosis detection

LysoTracker Red DND-99 (Thermo Fisher Scientific, lot L7528) was diluted to 2 μM in DMEM containing 50% rat serum. Embryos were

placed in media and incubated in a roller culture apparatus for 1 hour. The temperature was maintained at 37°C with 5% CO_2. Embryos were washed three times with phosphate-buffered saline (PBS) after staining to remove LysoTracker surplus and then fixed overnight in 4% paraformaldehyde in PBS followed by three washes for 5 min in PBS. Images were acquired using the light sheet microscope (Zeiss Lightsheet Z.1) at ×20 magnification, and analysis was performed using Imaris.

Supplementary Materials

The PDF file includes:
Supplementary Note
Table S1
Legends for movies S1 to S3
Figs. S1 to S5
References

Other Supplementary Material for this manuscript includes the following:
Movies S1 to S3

REFERENCES AND NOTES

1. A. Mongera, P. Rowghanian, H. J. Gustafson, E. Shelton, D. A. Kealhofer, E. K. Carn, F. Serwane, A. A. Lucio, J. Giammona, O. Campàs, A fluid-to-solid jamming transition underlies vertebrate body axis elongation. *Nature* **561**, 401–405 (2018).
2. E. H. Barriga, K. Franze, G. Charras, R. Mayor, Tissue stiffening coordinates morphogenesis by triggering collective cell migration in vivo. *Nature* **554**, 523–527 (2018).
3. M. Zhu, H. Tao, M. Samani, M. Luo, X. Wang, S. Hopyan, Y. Sun, Spatial mapping of tissue properties in vivo reveals a 3D stiffness gradient in the mouse limb bud. *Proc. Natl. Acad. Sci. U.S.A.* **117**, 4781–4791 (2020).
4. E. Hannezo, C. P. Heisenberg, Mechanochemical feedback loops in development and disease. *Cell* **178**, 12–25 (2019).
5. C. Parada, S. P. Banavar, P. Khalilian, S. Rigaud, A. Michaut, Y. Liu, D. M. Joshy, O. Campàs, J. Gros, Mechanical feedback defines organizing centers to drive digit emergence. *Dev. Cell* **57**, 854–866.e6 (2022).
6. M. Zhu, B. Gu, E. C. Thomas, Y. Huang, Y.-K. Kim, H. Tao, T. M. Yung, X. Chen, K. Zhang, E. K. Woolaver, M. R. Nevin, X. Huang, R. Winklbauer, J. Rossant, Y. Sun, S. Hopyan, A fibronectin gradient remodels mixed-phase mesoderm. *Sci. Adv.* **10**, eadl6366 (2024).
7. H. Tao, M. Zhu, K. Lau, O. K. W. Whitley, M. Samani, X. Xiao, X. X. Chen, N. A. Hahn, W. Liu, M. Valencia, M. Wu, X. Wang, K. D. Fenelon, C. C. Pasiliao, D. Hu, J. Wu, S. Spring, J. Ferguson, E. P. Karuna, R. M. Henkelman, A. Dunn, H. Huang, H. Y. H. Ho, R. Atit, S. Goyal, Y. Sun, S. Hopyan, Oscillatory cortical forces promote three dimensional cell intercalations that shape the murine mandibular arch. *Nat. Commun.* **10**, 1703 (2019).
8. F. Serwane, A. Mongera, P. Rowghanian, D. A. Kealhofer, A. A. Lucio, Z. M. Hockenbery, O. Campàs, In vivo quantification of spatially varying mechanical properties in developing tissues. *Nat. Methods* **14**, 181–186 (2017).
9. A. D'Angelo, K. Dierkes, C. Carolis, G. Salbreux, J. Solon, In vivo force application reveals a fast tissue softening and external friction increase during early embryogenesis. *Curr. Biol.* **29**, 1564–1571.e6 (2019).
10. M. Zhu, K. Zhang, H. Tao, S. Hopyan, Y. Sun, Magnetic micromanipulation for in vivo measurement of stiffness heterogeneity and anisotropy in the mouse mandibular arch. *Research* **2020**, 7914074 (2020).
11. K. Bambardekar, R. Clément, O. Blanc, C. Chardès, P.-F. Lenne, Direct laser manipulation reveals the mechanics of cell contacts in vivo. *Proc. Natl. Acad. Sci. U.S.A.* **112**, 1416–1421 (2015).
12. K. Zhang, M. Zhu, E. Thomas, S. Hopyan, Y. Sun, Existing and potential applications of elastography for measuring the viscoelasticity of biological tissues in vivo. *Front. Phys.* **9**, 670571 (2021).
13. R. Prevedel, A. Diz-Muñoz, G. Ruocco, G. Antonacci, Brillouin microscopy: An emerging tool for mechanobiology. *Nat. Methods* **16**, 969–977 (2019).
14. I. Kabakova, J. Zhang, Y. Xiang, S. Caponi, A. Bilenca, J. Guck, G. Scarcelli, Brillouin microscopy. *Nat. Rev. Methods Primers* **4**, 8 (2024).
15. G. Scarcelli, W. J. Polacheck, H. T. Nia, K. Patel, A. J. Grodzinsky, R. D. Kamm, S. H. Yun, Noncontact three-dimensional mapping of intracellular hydromechanical properties by Brillouin microscopy. *Nat. Methods* **12**, 1132–1134 (2015).
16. R. Schlüßler, S. Möllmert, S. Abuhattum, G. Cojoc, P. Müller, K. Kim, C. Möckel, C. Zimmermann, J. Czarske, J. Guck, Mechanical mapping of spinal cord growth and repair in living zebrafish larvae by brillouin imaging. *Biophys. J.* **115**, 911–923 (2018).
17. L. Martinez-Vidal, C. Testi, E. Pontecorvo, F. Pederzoli, E. Alchera, I. Locatelli, C. Venegoni, A. Spinelli, R. Lucianò, A. Salonia, A. Podestà, G. Ruocco, M. Alfano, Progressive alteration of murine bladder elasticity in actinic cystitis detected by Brillouin microscopy. *Sci. Rep.* **14**, 1–16 (2024).
18. S. Möllmert, M. Gutmann, P. Müller, K. Kim, J. B. Salvador, S. Aif, L. Meinel, J. Guck, Beyond comparison: Brillouin microscopy and AFM-based indentation reveal divergent insights into the mechanical profile of the murine retina. *bioRxiv*, 2024.01.24.577013 (2024).
19. R. Schlüßler, K. Kim, M. Nötzel, A. Taubenberger, S. Abuhattum, T. Beck, P. Müller, S. Maharana, G. Cojoc, S. Girardo, A. Hermann, S. Alberti, J. Guck, Correlative all-optical quantification of mass density and mechanics of sub-cellular compartments with fluorescence specificity. *Elife* **11**, e68490 (2022).
20. P. J. Wu, I. V. Kabakova, J. W. Ruberti, J. M. Sherwood, I. E. Dunlop, C. Paterson, P. Török, D. R. Overby, Water content, not stiffness, dominates Brillouin spectroscopy measurements in hydrated materials. *Nat. Methods* **15**, 561–562 (2018).
21. G. Scarcelli, S. H. Yun, Reply to 'Water content, not stiffness, dominates Brillouin spectroscopy measurements in hydrated materials. *Nat. Methods* **15**, 562–563 (2018).
22. V. Y. Zaitsev, A. L. Matveyev, L. A. Matveev, A. A. Sovetsky, M. S. Hepburn, A. Mowla, B. F. Kennedy, Strain and elasticity imaging in compression optical coherence elastography: The two-decade perspective and recent advances. *J. Biophotonics* **14**, e202000257 (2021).
23. J. Ophir, I. Céspedes, H. Ponnekanti, Y. Yazdi, X. Li, Elastography: A quantitative method for imaging the elasticity of biological tissues. *Ultrason. Imaging* **13**, 111–134 (1991).
24. J. M. Schmitt, OCT elastography: Imaging microscopic deformation and strain of tissue. *Opt. Express* **3**, 199–211 (1998).
25. K. M. Kennedy, L. Chin, R. A. McLaughlin, B. Latham, C. M. Saunders, D. D. Sampson, B. F. Kennedy, Quantitative micro-elastography: Imaging of tissue elasticity using compression optical coherence elastography. *Sci. Rep.* **5**, 15538 (2015).
26. K. M. Kennedy, C. Ford, B. F. Kennedy, M. B. Bush, D. D. Sampson, Analysis of mechanical contrast in optical coherence elastography. *J. Biomed. Opt.* **18**, 121508 (2013).
27. S. Yoshida, *Waves: Fundamentals and Dynamics* (Morgan & Claypool Publishers; 2017).
28. A. Tang, G. Cloutier, N. M. Szeverenyi, C. B. Sirlin, Ultrasound elastography and MR elastography for assessing liver fibrosis: Part 1, principles and techniques. *Am. J. Roentgenol.* **205**, 22–32 (2015).
29. R. Loomba, J. Cui, T. Wolfson, W. Haufe, J. Hooker, N. Szeverenyi, B. Ang, A. Bhatt, K. Wang, H. Aryafar, C. Behling, M. A. Valasek, G. Y. Lin, A. Gamst, D. A. Brenner, M. Yin, K. J. Glaser, R. L. Ehman, C. B. Sirlin, Novel 3D magnetic resonance elastography for the noninvasive diagnosis of advanced fibrosis in NAFLD: A prospective study. *Am. J. Gastroenterol.* **111**, 986–994 (2016).
30. P. Grasland-Mongrain, A. Zorgani, S. Nakagawa, S. Bernard, L. G. Paim, G. Fitzharris, S. Catheline, G. Cloutier, Ultrafast imaging of cell elasticity with optical microelastography. *Proc. Natl. Acad. Sci. U.S.A.* **115**, 861–866 (2018).
31. B. Gu, E. Posfai, J. Rossant, Efficient generation of targeted large insertions by microinjection into two-cell-stage mouse embryos. *Nat. Biotechnol.* **36**, 632–637 (2018).
32. S. Zörner, M. Kaltenbacher, R. Lerch, A. Sutor, M. Döllinger, Measurement of the elasticity modulus of soft tissues. *J. Biomech.* **43**, 1540–1545 (2010).
33. J. M. Walker, A. M. Myers, M. D. Schluchter, V. M. Goldberg, A. I. Caplan, J. A. Berilla, J. M. Mansour, J. F. Welter, Nondestructive evaluation of hydrogel mechanical properties using ultrasound. *Ann. Biomed. Eng.* **39**, 2521–2530 (2011).
34. K. McDole, L. Guignard, F. Amat, A. Berger, G. Malandain, L. A. Royer, S. C. Turaga, K. Branson, P. J. Keller, In toto imaging and reconstruction of post-implantation mouse development at the single-cell level. *Cell* **175**, 859–876.e33 (2018).
35. S. T. Thurman, M. Guizar-Sicairos, J. R. Fienup, Efficient subpixel image registration algorithms. *Opt. Lett.* **33**, 156–158 (2008).
36. Ł. Ambroziński, S. Song, S. J. Yoon, I. Pelivanov, D. Li, L. Gao, T. T. Shen, R. K. Wang, M. O'Donnell, Acoustic micro-tapping for non-contact 4D imaging of tissue elasticity. *Sci. Rep.* **6**, 38967 (2016).
37. M. A. Kirby, I. Pelivanov, G. Regnault, J. J. Pitre, R. T. Wallace, M. O'Donnell, R. K. Wang, T. T. Shen, Acoustic micro-tapping optical coherence elastography to quantify corneal collagen cross-linking: An ex vivo human study. *Ophthalmol. Sci.* **3**, 100257 (2023).
38. M. S. Taljanovic, L. H. Gimber, G. W. Becker, L. D. Latt, A. S. Klauser, D. M. Melville, L. Gao, R. S. Witte, Shear-wave elastography: Basic physics and musculoskeletal applications. *Radiographics* **37**, 855–870 (2017).
39. J. Burgess, J. T. Burrows, R. Sadhak, S. Chiang, A. Weiss, C. D'Amata, A. M. Molinaro, S. Zhu, M. Long, C. Hu, H. M. Krause, B. J. Pearson, An optimized QF-binary expression system for use in zebrafish. *Dev. Biol.* **465**, 144–156 (2020).
40. K. Lau, H. Tao, H. Liu, J. Wen, K. Sturgeon, N. Sorfazlian, S. Lazic, J. T. A. Burrows, M. D. Wong, D. Li, S. Deimling, B. Ciruna, I. Scott, C. Simmons, R. M. Henkelman, T. Williams, A. K. Hadjantonakis, R. Fernandez-Gonzalez, Y. Sun, S. Hopyan, Anisotropic stress orients remodelling of mammalian limb bud ectoderm. *Nat. Cell Biol.* **17**, 569–579 (2015).
41. D. Bi, J. H. Lopez, J. M. Schwarz, M. L. Manning, A density-independent rigidity transition in biological tissues. *Nat. Phys.* **11**, 1074–1079 (2015).

42. J. A. Martin, D. G. Schmitz, A. C. Ehlers, M. S. Allen, D. G. Thelen, Calibration of the shear wave speed-stress relationship in ex vivo tendons. *J. Biomech.* **90**, 9–15 (2019).
43. G. Captur, R. Wilson, M. F. Bennett, G. Luxán, A. Nasis, J. L. de la Pompa, J. C. Moon, T. J. Mohun, Morphogenesis of myocardial trabeculae in the mouse embryo. *J. Anat.* **229**, 314–325 (2016).
44. G. del Monte-Nieto, M. Ramialison, A. A. S. Adam, B. Wu, A. Aharonov, G. D'uva, L. M. Bourke, M. E. Pitulescu, H. Chen, J. L. de la Pompa, W. Shou, R. H. Adams, S. K. Harten, E. Tzahor, B. Zhou, R. P. Harvey, Control of cardiac jelly dynamics by NOTCH1 and NRG1 defines the building plan for trabeculation. *Nature* **557**, 439–445 (2018).
45. A. G. Cairelli, A. Gendernalik, W. X. Chan, P. Nguyen, J. Vermot, J. Lee, D. Bark, C. H. Yap, Role of tissue biomechanics in the formation and function of myocardial trabeculae in zebrafish embryos. *J. Physiol.* **602**, 597–617 (2024).
46. J. M. Cho, M. L. Steve Poon, E. Zhu, J. Wang, J. T. Butcher, T. Hsiai, Quantitative 4D imaging of biomechanical regulation of ventricular growth and maturation. *Curr. Opin. Biomed. Eng.* **26**, 100438 (2023).
47. L. A. Taber, G. I. Zahalak, Theoretical model for myocardial trabeculation. *Dev. Dyn.* **220**, 226–237 (2001).
48. B. A. de Boer, J. F. Le Garrec, V. M. Christoffels, S. M. Meilhac, J. M. Ruijter, Integrating multi-scale knowledge on cardiac development into a computational model of ventricular trabeculation. *Wiley Interdiscip. Rev. Syst. Biol. Med.* **6**, 389–397 (2014).
49. A. G. Cairelli, R. W. Y. Chow, J. Vermot, C. H. Yap, Fluid mechanics of the zebrafish embryonic heart trabeculation. *PLoS Comput. Biol.* **18**, e1010142 (2022).
50. K. Otomo, T. Omura, Y. Nozawa, S. J. Edwards, Y. Sato, Y. Saito, S. Yagishita, H. Uchida, Y. Watakabe, K. Naitou, R. Yanai, N. Sahara, S. Takagi, R. Katayama, Y. Iwata, T. Shiokawa, Y. Hayakawa, K. Otsuka, H. Watanabe-Takano, Y. Haneda, S. Fukuhara, M. Fujiwara, T. Nii, C. Meno, N. Takeshita, K. Yashiro, J. M. Rosales Rocabado, M. Kaku, T. Yamada, Y. Oishi, H. Koike, Y. Cheng, K. Sekine, J. I. Koga, K. Sugiyama, K. Kimura, F. Karube, H. Kim, I. Manabe, T. Nemoto, K. Tainaka, A. Hamada, H. Brismar, E. A. Susaki, descSPIM: An affordable and easy-to-build light-sheet microscope optimized for tissue clearing techniques. *Nat. Commun.* **15**, 4941 (2024).
51. K. B. Patel, W. Liang, M. J. Casper, V. Voleti, W. Li, A. J. Yagielski, H. T. Zhao, C. Perez Campos, G. S. Lee, J. M. Liu, E. Philipone, A. J. Yoon, K. P. Olive, S. M. Coley, E. M. C. Hillman, High-speed light-sheet microscopy for the in-situ acquisition of volumetric histological images of living tissue. *Nat. Biomed. Eng.* **6**, 569–583 (2022).
52. B. Gu, B. Bradshaw, M. Zhu, Y. Sun, S. Hopyan, J. Rossant, Live imaging YAP signalling in mouse embryo development. *Open Biol.* **12**, 210335 (2022).
53. Y. R. Lewis-Israeli, A. H. Wasserman, M. A. Gabalski, B. D. Volmert, Y. Ming, K. A. Ball, W. Yang, J. Zou, G. Ni, N. Pajares, X. Chatzistavrou, W. Li, C. Zhou, A. Aguirre, Self-assembling human heart organoids for the modeling of cardiac development and congenital heart disease. *Nat. Commun.* **12**, 5142 (2021).
54. N. Gjorevski, C. M. Nelson, Mapping of mechanical strains and stresses around quiescent engineered three-dimensional epithelial tissues. *Biophys. J.* **103**, 152–162 (2012).
55. M. Weber, N. Scherf, A. M. Meyer, D. Panáková, P. Kohl, J. Huisken, Cell-accurate optical mapping across the entire developing heart. *Elife* **6**, e28307 (2017).
56. E. Steed, N. Faggianelli, S. Roth, C. Ramspacher, J. P. Concordet, J. Vermot, *klf2a* couples mechanotransduction and zebrafish valve morphogenesis through fibronectin synthesis. *Nat. Commun.* **7**, 11646 (2016).
57. G. R. Kale, X. Yang, J. M. Philippe, M. Mani, P. F. Lenne, T. Lecuit, Distinct contributions of tensile and shear stress on E-cadherin levels during morphogenesis. *Nat. Commun.* **9**, 5021 (2018).
58. N. Baeyens, C. Bandyopadhyay, B. G. Coon, S. Yun, M. A. Schwartz, Endothelial fluid shear stress sensing in vascular health and disease. *J. Clin. Invest.* **126**, 821–828 (2016).
59. H. J. Lee, M. F. Diaz, K. M. Price, J. A. Ozuna, S. Zhang, E. M. Sevick-Muraca, J. P. Hagan, P. L. Wenzel, Fluid shear stress activates YAP1 to promote cancer cell motility. *Nat. Commun.* **8**, 14122 (2017).
60. D. Lachowski, E. Cortes, B. Robinson, A. Rice, K. Rombouts, A. E. Del Río Hernández, FAK controls the mechanical activation of YAP, a transcriptional regulator required for durotaxis. *FASEB J.* **32**, 1099–1107 (2018).
61. D. C. Lin, E. K. Dimitriadis, F. Horkay, Robust strategies for automated afm force curve analysis—I. Non-adhesive Indentation of soft, inhomogeneous materials. *J. Biomech. Eng.* **129**, 430–440 (2007).
62. A. Ahmad, J. Kim, N. A. Sobh, N. D. Shemonski, S. A. Boppart, K. J. Parker, M. M. Doyley, D. J. Rubens, B. F. Kennedy, K. M. Kennedy, D. D. Sampson, R. A. McLaughlin, S. J. Kirkpatrick, R. K. Wang, D. D. Duncan, A. Baranov, J. Li, S. Emelianov, K. V. Larin, Magnetomotive optical coherence elastography using magnetic particles to induce mechanical waves. *Biomed. Opt. Express* **5**, 2349–2361 (2014).
63. J. E. Sader, Frequency response of cantilever beams immersed in viscous fluids with applications to the atomic force microscope. *J. Appl. Phys.* **84**, 64–76 (1998).
64. W. T. Thomson, M. D. Dahleh, *Theory of Vibrations with Applications* (Pearson; 2014).
65. G. R. Cowper, The shear coefficient in timoshenko's beam theory. *J. Appl. Mech.* **33**, 335–340 (1966).
66. V. Giurgiutiu, *Structural health monitoring with piezoelectric wafer active sensors* (Elsevier; 2007).
67. B. A. Auld, *Acoustic fields and Waves in Solids* (R.E. Krieger; 1990), vol. 2.
68. C. E. Repetto, A. Roatta, R. J. Welti, Forced vibrations of a cantilever beam. *Eur. J. Phys.* **33**, 1187–1195 (2012).
69. C. Balleyguier, L. Ciolovan, S. Ammari, S. Canale, S. Sethom, R. Al Rouhbane, P. Vielh, C. Dromain, Breast elastography: The technical process and its applications. *Diagn. Interv. Imaging* **94**, 503–513 (2013).
70. S. K. Venkatesh, M. Yin, R. L. Ehman, Magnetic resonance elastography of liver: Technique, analysis, and clinical applications. *J. Magn. Reson. Imaging* **37**, 544–555 (2013).

Acknowledgments: We thank T. Cui for help with mechanics analysis and S. Saber for help with DMEM viscosity measurement. **Funding:** This work was funded by the Canada First Research Excellence Fund/Medicine by Design (MbDGQ-2021-04 to S.H. and Y.S. and MPDF-2020-04 to M.Z.) and the Canadian Institutes of Health Research (168992) to S.H. and Y.S. Y.S. also acknowledges support from the Canada Research Chairs program. **Author contributions:** M.Z. and K.Z. designed and performed the experiments and modeling and wrote the manuscript; E.C.T. wrote the tracking program. R.X and B.C. provided zebrafish experimental support. M.Z., Y.S., and S.H. co-conceived the project. Y.S. and S.H. cofunded the project and edited the manuscript. **Competing interests:** The authors declare that they have no competing interests. **Data and materials availability:** The data that support the findings of this study are available at https://figshare.com/articles/dataset/light_sheet_elastography/26818240. All custom codes used in this paper are available at https://zenodo.org/uploads/14434614 and https://github.com/MinZhuUOTSickKids/light_sheet_elastography.

Submitted 9 October 2024
Accepted 6 February 2025
Published 14 March 2025
10.1126/sciadv.adt7274